Blind Source Separation of Inspiration and Expiration in Respiratory sEMG Signals

Julia Sauer[1], Merle Streppel[1], Niklas M. Carbon[2], Eike Petersen[3] and Philipp Rostalski[1]

[1]Institute for Electrical Engineering in Medicine, Universität zu Lübeck, Ratzeburger Allee 160, 23562 Lübeck, Germany.
[2]Charité – Universitätsmedizin Berlin, corporate member of Freie Universität Berlin and Humboldt Universität zu Berlin, Department of Anesthesiology and Intensive Care Medicine, Augustenburger Platz 1, 13353 Berlin, Germany.
[3]DTU Compute, Technical University of Denmark, Kgs. Lyngby, Denmark

E-mail: `j.sauer@uni-luebeck.de`

Keywords: Respiration, Surface electromyography, Nonnegative matrix factorization, Stationary wavelet transform, Blind source separation, Underdetermined, Unsupervised

Abstract.

Objective: Surface electromyography (sEMG) is a noninvasive option for monitoring respiratory effort in ventilated patients. However, respiratory sEMG signals are affected by crosstalk and cardiac activity. This work addresses the blind source separation (BSS) of inspiratory and expiratory electrical activity in single- or two-channel recordings. The main contribution of the presented methodology is its applicability to the addressed muscles and the number of available channels.

Approach: We propose a two-step procedure consisting of a single-channel cardiac artifact removal algorithm, followed by a single- or multi-channel BSS stage. First, cardiac components are removed in the wavelet domain. Subsequently, a nonnegative matrix factorization (NMF) algorithm is applied to the envelopes of the resulting wavelet bands. The NMF is initialized based on simultaneous standard pneumatic measurements of the ventilated patient.

Main results: The proposed estimation scheme is applied to twelve clinical datasets and simulated sEMG signals of the respiratory system. The results on the clinical datasets are validated based on expert annotations using invasive pneumatic measurements. In the simulation, three measures evaluate the separation success: The distortion and the correlation to the known ground truth and the inspiratory-to-expiratory signal power ratio. We find an improvement across all SNRs, recruitment patterns, and channel configurations. Moreover, our results indicate that the initialization strategy replaces the manual matching of sources after the BSS.

Significance: The proposed separation algorithm facilitates the interpretation of respiratory sEMG signals. In crosstalk affected measurements, the developed method may help clinicians distinguish between inspiratory effort and other muscle activities using only noninvasive measurements.

1. Introduction

The possibility of noninvasive measurements makes surface electromyography (sEMG) valuable in clinical applications. Compared to invasive setups with needle electrodes,

recorded electrical potentials on the skin surface result from superimposing all nearby electrical fields. This provides the opportunity to record the electrical activity of multiple muscle fibers with a single channel. A limitation of surface measurements is that crosstalk from nearby tissues and undesired surrounding electrical sources often cannot be avoided. Bipolar configurations with great inter-electrode distance, which previous works have used in respiratory settings [1], [2], enhance this effect [3].

These properties must be considered while interpreting sEMG recordings, and one approach is blind source separation (BSS). The application of BSS to different types of sEMG signals and in the context of various applications is a widely studied field. For a recent review, refer to the publication by Holobar and Farina [4]. BSS generally targets the reconstruction of source signals, using no prior knowledge about the sources or the parameters of the underlying system. When applied to sEMG measurements, BSS algorithms differ in the desired domain or the level of detail of the separation. At the smallest scale, electrical signals of single motor units (MUs) are reconstructed [5]–[7]. Furthermore, BSS may identify the contribution of single muscles to suppress crosstalk [8], [9]. And finally, the interaction of multiple muscles in complex motion patterns could be characterized [4], [10]. The latter is especially popular in myoelectric control of prostheses and aims to identify muscle synergies [11]–[18]. These approaches differ in the assumptions on the underlying mixing process, with convolutive and instantaneous linear mixture models being the most frequent assumptions [4].

Most BSS algorithms in the context of sEMG require an equal or larger number of channels than sources [4]. The algorithm proposed in this article targets the separation of inspiratory and expiratory activity in single-channel and low-density sEMG recordings of the respiratory muscles. This application is similar to the earlier contribution by Petersen *et al.* [9]. In contrast to high-density measurements, the number of channels is small in low-density recordings and each electrode is placed next to a particular muscle of interest or at a defined anatomical position. As a consequence, the number of channels might not exceed the number of sources in this setup. Especially the single-channel case is underdetermined. However, these configurations are compatible with routine use in the intensive care setting. If not corrupted by crosstalk, these measurements allow for monitoring respiratory activity [19], detecting patient-ventilator asynchrony [20]–[22] and evaluating the patient's work of breathing [1], [2], [23].

Several muscles contribute to breathing. The primary muscle of inspiration is the diaphragm, a large muscle that horizontally spans a significant part of the thorax. Accessorily, the external intercostal muscles can support the inspiratory effort. Expiration is generally passive at rest. However, in stress or ill-configured ventilatory support, the abdominal and internal intercostal muscles enforce active expiration [24]. From the perspective of skin electrodes, the rib cage, abdominal muscles and fat partly cover the diaphragm, such that the electrode-to-muscle distance is large. Hence, low signal amplitudes and crosstalk must be expected in sEMG recordings of the diaphragm. External and internal intercostals are anatomically similar and positioned close to one another, also leading to a high probability of crosstalk being present in the recordings. Besides, the heart's electrical activity heavily contaminates all sEMG measurements on the thorax [25]–[27]. In conclusion, these hindrances make a blind separation of inspiratory and expiratory activity quite specific and challenging.

Our proposed approach targets the estimation of the respiratory muscle drive, which Holobar and Farina [4] call an *activation primitive*. We assume that two

primitives can serve as surrogates for the sEMG signal envelopes of two virtual sources or synergies: *inspiration* and *expiration*. As multiple muscles contribute to the respiratory sEMG signals, this concept aggregates their synergistic effect and does not claim to identify the activity profiles of individual muscles. We chose nonnegative matrix factorization (NMF) [28] for this task of blind source separation and assume a linear and instantaneous mixing process of the source activation primitives.

Validation is performed in two different domains. On the one hand, the proposed procedure is applied to clinical datasets recorded in ventilated patients and evaluated based on experts' annotations. On the other hand, simulated sEMG datasets of all relevant respiratory muscles and cardiac activity are used for quantitative assessment since ground truth for the separate source signals is not accessible in clinical recordings. Therefore, we use a simulation model for sEMG signals [29], [30] complemented by an ECG simulator [31], [32] and a pneumatic model of the respiratory system [33].

The central contribution of this work is an algorithm to reduce crosstalk in clinical respiratory sEMG recordings. An important feature is its applicability to a limited number of recording channels, including the underdetermined case. To the best of the author's knowledge, no state-of-the-art approach exists for the problem at hand. Specifically, this work refines a method for suppressing cardiac activity [27] and interfaces the results to a BSS algorithm. The latter employs the NMF algorithm as a tool for identifying muscle synergies [4], [10]–[18], [34]–[37]. Here this work contributes in three ways. First, activation primitives for inspiration and expiration are identified reliably. Second, underdetermination is overcome by using a denoised wavelet representation of the signals. Third, an initialization strategy based on pneumatic recordings of the ventilated patient's respiratory airflow is introduced. It is shown that this approach allows unsupervised and automated source matching and thus contributes to the applicability in the clinical context. Compared to Petersen *et al.* [9], who have also addressed the application of BSS algorithms to respiratory sEMG recordings, the above contributions represent the main difference and major innovation. Additionally, the validation is based on a larger simulation model, including the intercostal muscles, and the algorithm's performance on clinical datasets is also evaluated quantitatively using expert knowledge.

The following section describes the clinical datasets and the sEMG simulation setup, as well as the overall processing algorithm and the applied validation procedure. The separation results on simulated and real signals are provided in section 3 and discussed in section 4.

2. Methods

The proposed algorithm performs cardiac artifact removal prior to the blind separation of respiratory muscle activities. Both processing steps use dimensionality expansion based on the stationary wavelet transform (SWT) [38]. Petersen *et al.* [27] have proposed that using the SWT for cardiac artifact removal can be beneficial for certain applications. Other established tools like the Pan-Tompkins algorithm [39], wavelet-thresholding [40], and NMF [28] are used for this purpose. The BSS step is complemented by an initialization strategy that allows an automatic source matching based on airflow measurements of the ventilated patients. The unsupervised procedure separates inspiratory and expiratory sEMG activity from single- and multi-channel recordings with dominant cardiac artifacts. To be precise, the activation primitives [4] of inspiration and expiration are estimated. The algorithm is tested on clinical datasets

and simulated sEMG signals. The latter enables a proper validation based on the known ground truth.

This section describes the acquisition of the utilized respiratory sEMG data, first the clinical and subsequently the simulation setup. The next part of this section outlines the overall algorithm. The final section details the quantitative validation applied to the separation results.

2.1. Data acquisition

2.1.1. Clinical datasets. Clinical data were obtained from twelve adult intensive care patients enrolled in an observational trial at Charité, Universitätsmedizin Berlin, Department of Anesthesiology and Operative Intensive Care Medicine (trial registry number DRKS00017138). All patients were treated with assisted mechanical ventilation due to acute respiratory distress syndrome. Measurements were performed during several stages of illness for 15 min to 30 min per recording and captured pneumatic data, including respiratory airflow, the transdiaphragmatic pressure, and two differential sEMG signals. Figure 1 illustrates the electrode positions used for channel A and channel B. The electrodes for channel A are placed at the costal margin, measuring the electrical activity of the diaphragm and the abdominal muscles. For channel B, electrodes are placed parasternally in the third intercostal space measuring intercostal muscles. In this work, BSS is applied to sections of 30 s, one for each patient. These segments were selected by manual inspection and show the patient's respiratory effort with electrical activity in at least one sEMG channel.

2.1.2. sEMG signal simulation. A simulation allows accessing the ground truth since the activity of each contributing source and the source signals are known. No physiological measurement enables the measuring of this ground truth *in vivo* [6], [7], [9]. Thus, applying the proposed algorithm to simulated data is crucial for validating the source separation results.

The simulation is based on a comprehensive model for simulating sEMG recordings of skeletal muscles as proposed by Petersen and Rostalski [29], implemented in the *semgsim* toolbox [30]. The model comprises, for instance, motor unit pool organization, rate coding and recruitment, intracellular action potential generation in the signal creation and the propagation of these action potentials throughout the surrounding biological tissue layers. A realistic EMG-force relationship to the whole muscle as well as to individual MUs is assumed. Moreover, the model conforms with experimentally observed phenomena such as the size principle [41], [42], and the onion-skin phenomenon [43], [44]. A superposition of many spatially filtered motor unit action potentials yields the overall surface potential. The effect of the surrounding biological tissues is simulated based on the analytical model of Farina and Merletti [45], which represents muscle fibers as straight lines that run parallel to the skin surface in an infinitely extended, three-layer volume conductor. In addition to this geometrical simplification, the model also does not account for muscle shortening or muscular fatigue effects.

The considered surface electrodes and their positions are based on the clinical setting and agree with the illustration in fig. 1, showing the two measuring channels (A and B). Figure 1 also visualizes the approximated shapes of the muscles used in the simulation. The diaphragm (DI) functions as the primary muscle of inspiration. Moreover, one pair of the external (EI) and internal intercostal (II) muscles are

included as accessory respiratory muscles. The EI are active in inspiration and the II in expiration. Furthermore, six identical packs model the rectus abdominus (RA), which acts as an expiratory muscle. The number of MUs for each simulated muscle was chosen as follows: Each of the intercostal muscle pairs consists of 80 MUs, while the diaphragm comprises 200 MUs. Lastly, each of the RA packs contains 50 MUs. Across all muscles, more than 400,000 individual muscle fibers were simulated. For positioning the MUs, each muscle's cross-section was evenly divided into a set of rectangular parts, and a corresponding fraction of the muscle's MUs were then distributed randomly within each part. The simulation uses the muscle activity patterns shown in the first row of fig. 4, representing eight breathing cycles with a respiratory rate of 15 breaths per minute.

Independently of the sEMG simulation, cardiac artifacts are generated using the ECG simulator published in the open-source ECG toolbox by Sameni [31]. The simulator is based on the ECG model by McSharry *et al.* [32]. The scaled simulated cardiac activity is added to the EMG simulations so that the power during QRS-complexes is a hundred times higher than the EMG power during active phases. This amplitude relation imitates the ECG-to-EMG ratio of the clinical data [27].

In the source separation algorithm described in the next section, pneumatic recordings are used for the initialization step. Hence, a pneumatic model extends the sEMG simulation to provide an equivalent validation dataset. The basis of this third simulation component is a single-compartment model [33] of the respiratory system, i. e.,

$$p_{\text{vent}}(t) + p_{\text{mus}}(t) = R\dot{V}(t) + \frac{1}{C}V(t) + p_0 \tag{1}$$

with the airway resistance R and the system compliance C. The pressure p_0 is the constant offset pressure within the lung, which is usually higher than the environmental pressure. The contraction of the respiratory muscles produces the time-varying pressure p_{mus}. We model p_{mus} by a weighted sum of sEMG envelope signals obtained from the acquired differential sEMG simulations as has been proposed by Petersen *et al.* [23]. Positive weights are chosen for inspiratory muscles, whereas muscles that enforce active expiration, contribute negatively. Hence, the pressure p_{mus} is positive during inspiration and negative during expiration. Additionally, a rectangular function with positive offset models the applied pressure of the ventilator p_{vent}. The pressure p_{mus} triggers the beginning of inspiration in p_{vent}, simulating an assisted ventilator mode. Finally, solving the linear differential equation eq. (1) for the volume V provides the desired airflow $\dot{V}$.

2.2. Algorithm for the separation of inspiration and expiration

The overall source separation pipeline is depicted in fig. 1, starting with the data acquisition on the top left and finishing with the estimated source signals on the right. The measurement setup is described above in section 2.1. It provides two sEMG recordings, where $\mathbf{s}_A$ is the differential signal of channel A corresponding to electrodes 1 and 2 and $\mathbf{s}_B$ refers to channel B of electrodes 3 and 4. The signal amplitudes vary widely depending on the patient's breathing effort, muscle recruitment, and electrode positioning. Sometimes, one of these channels contains no sEMG activity and thus is uninformative. Additionally, only one channel might be available or reliable in clinical practice due to disturbances and low signal quality. Therefore, this article contributes single- and multi-channel variants of the algorithm.

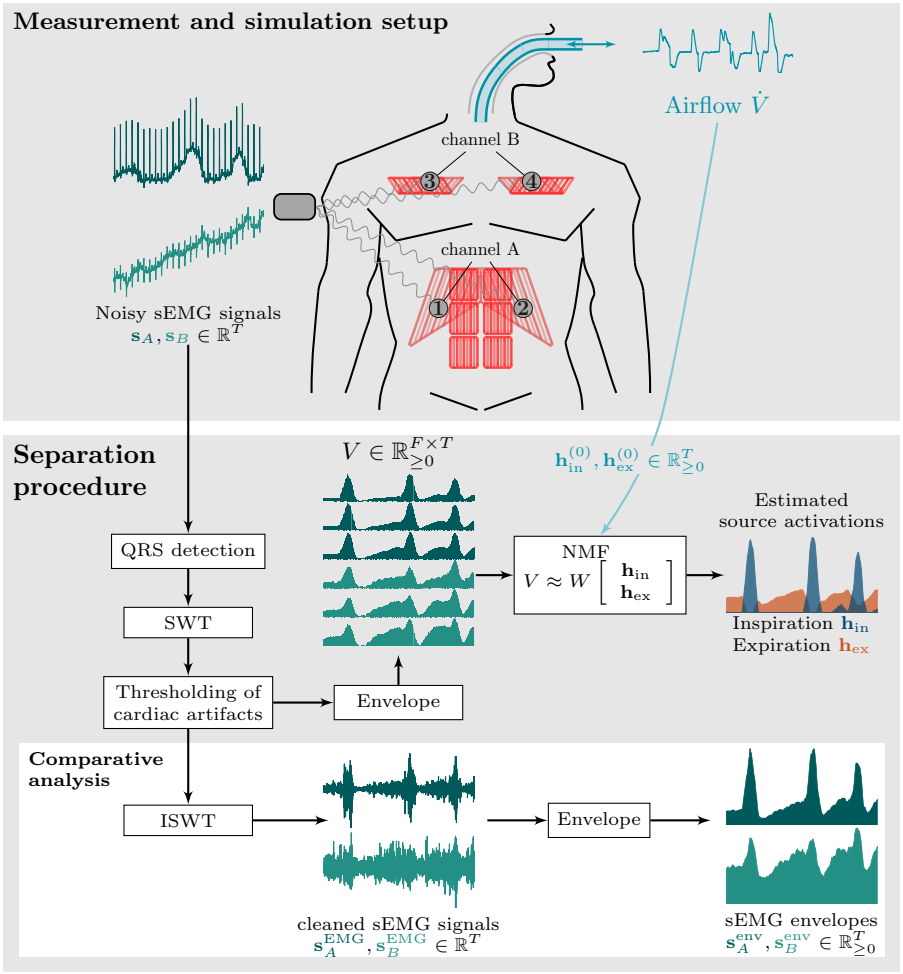

Figure 1: Overview of the signal processing algorithm. At the top, the anatomical scheme illustrates the experimental setup for clinical measurements and simulations. This includes the electrode positions and muscle model geometries. Next, the signal preprocessing and source separation is visualized: In noisy sEMG data, cardiac artifacts are suppressed. Subsequently, NMF is applied. In this step, the initialization of the NMF coefficients employs the respiratory airflow. The algorithm's outcomes are the source activation primitives $\mathbf{h}_{\text{in}}$ and $\mathbf{h}_{\text{ex}}$ corresponding to inspiration and expiration. Those can be compared to the sEMG envelope signals in which cardiac artifacts are removed, but respiratory muscle activities are still mixed.

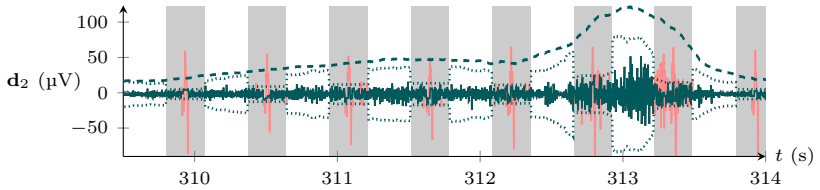

Figure 2: Cardiac artifact removal and feature extraction. This plot shows an extract of the second detail coefficient (—— $\mathbf{d}_2$) of an exemplary breath. The estimation of the *EMG level* (····· $\pm\mathbf{t}_2^{\mathrm{EMG}}$) takes into account the gates (▬) around the detected QRS-complexes. See section 2.2 for details. Subsequently, thresholding removes most of the cardiac artifact and yields the modified coefficient (—— $\mathbf{d}_2^{\mathrm{EMG}}$). Finally, its envelope (- - - $\mathbf{d}_2^{\mathrm{env}}$, here multiplied by ten) is extracted as one row of the feature matrix V.

While we have not yet tested its application to high-density sEMG measurements, our proposed algorithm can - in theory - be performed on an arbitrary number of simultaneously recorded channels as long as these recordings contain respiratory muscle activity. The signal separation procedure is subdivided into two phases. The first phase is cardiac artifact removal and feature extraction, performed individually for each recorded channel. In the second phase, an NMF algorithm is employed to perform the blind source separation using the extracted features of all available channels.

The first stage starts with applying the algorithm by Pan and Tompkin [39] to detect each heartbeat in a single cardiac contaminated sEMG recording $\mathbf{s} \in \mathbb{R}^T$, where T is the number of samples. Next, $\mathbf{s}$ is decomposed by the SWT [38] of level n

$$\mathrm{SWT}\{\mathbf{s}\} = \{\mathbf{d}_1, \ldots, \mathbf{d}_n, \mathbf{a}_n\} \tag{2}$$

using a second-order Daubechies Wavelet [27]. Here, $\mathbf{a}_n \in \mathbb{R}^T$ and $\mathbf{d}_i \in \mathbb{R}^T$ denote the nth approximation and the ith detail coefficient, respectively. These coefficients represent different frequency contents of $\mathbf{s}$, sorted from highest ($\mathbf{d}_1$) to lowest ($\mathbf{a}_n$) frequency component. The temporal resolution of the vectors $\mathbf{d}_1, \ldots, \mathbf{d}_n, \mathbf{a}_n$ matches the sampling of the recorded signal $\mathbf{s}$, which is an inherent property of the SWT. Our approach employs the detail coefficients to expand the feature space for overcoming underdetermination. As a result, separating two sources in the single-channel (underdetermined) case requires $n \geq 2$. We found that $n = 3$ is appropriate because the first three detail coefficients contain the most sEMG signal power. Higher-level wavelet coefficients cover lower-frequency signal components, such as cardiac artifacts and other disturbances. Hence, the first three detail coefficients provide meaningful information for the following source separation.

In classical wavelet denoising methods, a fixed or adaptive threshold is applied to each wavelet band [40]. This threshold denotes the noise level. Coefficients, which do not exceed the threshold are assumed to be noise and thus are not considered. The proposed approach of this article suppresses the cardiac content in the wavelet domain. Consequently, it removes sections where the coefficients exceed the threshold or time-varying *EMG level*. Figure 2 illustrates the thresholding procedure. Similar to [27], this threshold $\mathbf{t}_i^{\mathrm{EMG}} \in \mathbb{R}^T$ is calculated by first gating the cardiac artifacts in each detail coefficient $\mathbf{d}_i$ and then calculating the vector $\mathbf{d}_i^{\mathrm{med}}$ by applying a moving median filter (window width of 1 s) to the absolute values of each wavelet band. This filter does not consider gated samples close to QRS-complexes. Narrow gates are

chosen for low-level coefficients, as the cardiac residuals are sharper in these higher-frequency bands. Concretely, we start with gates of 250 ms in $\mathbf{d}_1$ and increase by 25 ms in every higher level. These gates can suppress P-waves, whereas slower T-waves are mostly mapped to the discarded, low-frequency band $\mathbf{a}_n$. Next, the *EMG level* $\mathbf{t}_i^{\mathrm{EMG}}$ is approximated by three times $\mathbf{d}_i^{\mathrm{med}}$ within the gates and ten times $\mathbf{d}_i^{\mathrm{med}}$ for the rest. These scales are set manually and work sufficiently well for common EMG-to-ECG ratios of thoracic sEMG recordings. In total, $\mathbf{d}_i^{\mathrm{EMG}} \in \mathbb{R}^T$ is the ith detail coefficient with suppressed cardiac artifacts, where samples are set to zero if they exceed $\mathbf{t}_i^{\mathrm{EMG}}$ or fall below $-\mathbf{t}_i^{\mathrm{EMG}}$. The thresholded wavelet bands $\mathbf{d}_i^{\mathrm{EMG}}$ are further used to build the feature matrix V required for the following NMF algorithm [28]. Usually, in applications of NMF to EMG signals, the EMG envelope (as opposed to the raw signal) is used [4], [10], [12]–[16], [34], [36], [37]. Similarly, we calculate the envelopes of $\mathbf{d}_i^{\mathrm{EMG}}$ in this approach by

$$\mathbf{d}_i^{\mathrm{env}} = \mathrm{env}(\mathbf{d}_i^{\mathrm{EMG}}) \in \mathbb{R}_{\geq 0}^T, \tag{3}$$

where the function env denotes a moving mean filter of the absolute value with a window of 750 ms.

The second phase of the algorithm employs the extracted features of all available sEMG recordings $\mathbf{s}_j \in \mathbb{R}^T$ with $j = 1, \ldots, m$ to create the nonnegative feature matrix V. The features of all channels are stacked as follows

$$V = [V_1, \ldots, V_m]^\top = \left[\mathbf{d}_{1,1}^{\mathrm{env}}, \ldots, \mathbf{d}_{n,m}^{\mathrm{env}}\right]^\top \in \mathbb{R}_{\geq 0}^{F \times T}, \tag{4}$$

where $\mathbf{d}_{i,j}^{\mathrm{env}}$ denotes the envelope of the ith modified detail coefficient extracted from jth recording channel. In the single-channel case, the number of features F complies with the number of levels n, and for multiple recordings, $F = m \cdot n$ applies. The feature matrix characterizes the contribution of all sources to each wavelet band over time. The actual NMF source separation

$$V \approx WH \quad \text{with } W \in \mathbb{R}_{\geq 0}^{F \times K} \text{ and } H \in \mathbb{R}_{\geq 0}^{K \times T} \tag{5}$$

is performed using an iterative optimization scheme [28], which provides the arbitrarily scaled matrices W and H. The algorithm requires the specification of the number of sources K and initialization of the basis matrix W and source activation matrix H. We target to separate the inspiratory and expiratory activation primitives, hence we choose $K = 2$. In the field of BSS in audio signal processing, the matrix W is often initialized or even fixed with previously learned basis vectors. This initialization requires isolated training data of the audio sources. However, in the respiratory sEMG context, this is inconvenient because it would either require calibration by the separate contraction of inspiratory and expiratory muscles or a manual segmentation. Additionally, we expect the source's basis vectors to vary between recordings and patients because of the high dimensional and complex physiological system reduced to F coefficients. Thus, an initialization of W with general basis vectors is not a reliable option, and W is initialized with uniformly distributed random positive numbers in $(0, 1)$ instead. However, as opposed to audio signal processing, prior information on the source activations H is available. This is the measured airflow $\dot{V}$, which flows through the patients' airways. A positive flow denotes inspiration and negative values expiration. Note that for ventilated patients, the ventilator support shapes $\dot{V}$ significantly, and it is well-known that there is a high prevalence of patient-ventilator asynchrony under assisted ventilation [20]. Therefore, the airflow is only a rough approximation of the source activations, because in $\dot{V}$ the timing and waveform

may differ from the sEMG activity. Still, it proved beneficial to initialize the matrix H by

$$H^{(0)} = \left[\mathbf{h}_{\text{in}}^{(0)}, \mathbf{h}_{\text{ex}}^{(0)}\right]^{\top} \in \mathbb{R}_{\geq 0}^{2\times T} \tag{6}$$

with the initial source activation vector of inspiration

$$\mathbf{h}_{\text{in}}^{(0)} = \begin{cases} \dot{V} & \text{if } \dot{V} > 0 \\ 0 & \text{else} \end{cases} + \boldsymbol{\nu}_1 \tag{7}$$

and the initialization of expiration

$$\mathbf{h}_{\text{ex}}^{(0)} = \begin{cases} |\dot{V}| & \text{if } \dot{V} < 0 \\ 0 & \text{else} \end{cases} + \boldsymbol{\nu}_2, \tag{8}$$

where $\boldsymbol{\nu}_1, \boldsymbol{\nu}_2 \in \mathbb{R}_{\geq 0}^{T}$ are random nonnegative vectors drawn from the uniform distribution $\mathcal{U}(0, \mathbb{E}\{|\dot{V}|\}/4)$.

Choosing $K = 2$ in the multi-channel case goes hand in hand with the assumption that

$$\mathbf{d}_{i,j}^{\text{env}} \approx w_{i,j}^{\text{in}}\mathbf{h}_{\text{in}} + w_{i,j}^{\text{ex}}\mathbf{h}_{\text{ex}} \quad \text{with } w_{i,j}^{\text{in}}, w_{i,j}^{\text{ex}} \geq 0. \tag{9}$$

Thus, both sources can project different spectral features onto each recording channel, represented in the basis vectors of the matrix

$$W = [\mathbf{w}_{\text{in}}, \mathbf{w}_{\text{ex}}] = \begin{bmatrix} w_{1,1}^{\text{in}} & w_{1,1}^{\text{ex}} \\ \vdots & \vdots \\ w_{n,m}^{\text{in}} & w_{n,m}^{\text{ex}} \end{bmatrix} \in \mathbb{R}_{\geq 0}^{F\times 2}. \tag{10}$$

This assumption is physiologically valid if all inspiratory muscles work synchronously, as well as all expiratory ones. It is also valid if mainly one muscle is dominant during inspiration or expiration in all channels. Additionally, it is robust against short irregularities because the envelopes of the wavelet bands are used and the optimization is performed on multiple breathing cycles. On the other hand, this approach assumes stationary source properties and no crosstalk by other muscles groups than the respiratory ones.

2.3. Evaluation of separation results

This work targets the estimation of the inspiratory and expiratory source activation primitives. For quantitative evaluation, the separation results $\mathbf{h}_{\text{in}}$ and $\mathbf{h}_{\text{ex}}$ are compared to the two references $\mathbf{r}_{\text{in}}$ and $\mathbf{r}_{\text{ex}}$. Due to the arbitrary scaling of the BSS results, both should be similar up to a scaling factor. In the multi-channel case, the similarity

$$\mathbf{r}_{\text{in},j} \approx \alpha_{\text{in},j}\mathbf{h}_{\text{in}} \quad \text{and} \quad \mathbf{r}_{\text{ex},j} \approx \alpha_{\text{ex},j}\mathbf{h}_{\text{ex}} \tag{11}$$

is assessed for all channels $j = 1, \ldots, m$ with the same two source activation primitives but channel-specific reference signals and scaling factors. Three evaluation measures are defined to quantify different properties of the separation results. All three are independent of absolute signal amplitudes. This section first describes an approach for determining the scaling factors in eq. (11). After that, the three utilized performance measures and the generation of multiple simulation-based test settings are explained. The latter includes the construction of the corresponding reference signals. Subsequently, we propose an approach to evaluating the algorithm's performance on clinical data.

2.3.1. Scaling factors. An inherent property of the NMF algorithm is that the scaling of basis and activation vectors is arbitrary. To determine a physically meaningful scaling, we assume an instantaneous mixture of the sources and specify scaling factors such that the linear combination of both estimated primitives

$$\mathbf{s}_j^{\text{env}} \approx \alpha_{\text{in},j}\mathbf{h}_{\text{in}} + \alpha_{\text{ex},j}\mathbf{h}_{\text{ex}} \quad \text{with } j = 1, \ldots, m \tag{12}$$

approximates the total respiratory muscle activity. The envelope signal $\mathbf{s}_j^{\text{env}} \in \mathbb{R}_{\geq 0}^T$ represents the superposition of all contributing respiratory muscle activities measured at jth channel. The lower branch of fig. 1 illustrates the process of calculating $\mathbf{s}_j^{\text{env}}$ based on the thresholded SWT coefficients. Applying the inverse stationary wavelet transform (ISWT) to the modified coefficient vectors of jth channel reconstructs the sEMG signal with suppressed cardiac artifacts

$$\mathbf{s}_j^{\text{EMG}} = \text{ISWT}\left\{\mathbf{d}_{1,j}^{\text{EMG}}, \ldots, \mathbf{d}_{n,j}^{\text{EMG}}, \mathbf{0}\right\} \in \mathbb{R}^T. \tag{13}$$

All samples of the highest approximation coefficient $\mathbf{a}_n$ are set to zero, assuming they do not contribute to the sEMG activity. For clarity, the difference between the noisy recording $\mathbf{s}_j$ and $\mathbf{s}_j^{\text{EMG}}$ corresponds to cardiac activity and other low-frequency disturbances. The sEMG envelope of jth channel

$$\mathbf{s}_j^{\text{env}} = \text{env}\left(\mathbf{s}_j^{\text{EMG}}\right) \in \mathbb{R}_{\geq 0}^T, \tag{14}$$

is calculated in the same way as the envelopes of wavelet bands in eq. (3). What is essential here is that $\mathbf{s}_1^{\text{env}}, \ldots, \mathbf{s}_m^{\text{env}}$ are independent of the BSS and still contain a mix of muscle activities. Additionally, they have a physiologically interpretable scale and unit. For each channel, two scaling factors in eq. (12) are determined by minimizing the squared error

$$\alpha_{\text{in},j}, \alpha_{\text{ex},j} = \text{argmin } ||\mathbf{s}_j^{\text{env}} - (\alpha_{\text{in},j}\mathbf{h}_{\text{in}} + \alpha_{\text{ex},j}\mathbf{h}_{\text{ex}})||_2^2 \tag{15}$$

with $\alpha_{\text{in},j}, \alpha_{\text{ex},j} \geq 0$. The implementation of the nonnegative least squares optimization is based on a FORTRAN solver published in [46], which satisfies the Karush-Kuhn-Tucker conditions. The approximation in eq. (12) assumes that the instantaneous mixture of the inspiratory and expiratory activation primitives fully represents the activity of all recruited respiratory muscles measured at all channels. This is a strong assumption, which could be violated by the nonlinear sEMG signal generation, and the presence of non-respiratory crosstalk.

2.3.2. Evaluation measures. Schobben *et al.* [47] proposed the *distortion* of $\mathbf{h}$ to measure the distance of the separated source signal $\mathbf{h}$ compared to its reference $\mathbf{r}$ by

$$E_{\text{dist}}(\mathbf{h}) = 10 \log\left(\frac{\mathbb{E}\left\{(\mathbf{r} - \alpha\mathbf{h})^2\right\}}{\mathbb{E}\left\{\mathbf{r}^2\right\}}\right) \quad \text{(dB)}, \tag{16}$$

which quantifies the relative signal power of the residuals with $\alpha = \mathbb{E}\{\mathbf{r}^2\}/\mathbb{E}\{\mathbf{h}^2\}$. This first measure E_{dist} considers the error of the BSS results. Other works quantified the separation performance by calculating the *correlation* [10], [11], [14], [37]. Hence, the second measure compares the source signal with its reference by

$$E_{\text{corr}}(\mathbf{h}) = f_{\text{corr}}(\mathbf{r}, \mathbf{h}), \tag{17}$$

where f_{corr} is the Pearson correlation coefficient.

We define a third measure for evaluating the separation success, which only considers an application-specific objective of the proposed algorithm: the separation

of inspiratory and expiratory activity. Therefore, each separated source signal's mean amplitude during inspiration $f_{\text{in}}(\mathbf{h})$ and during expiration $f_{\text{ex}}(\mathbf{h})$ are compared. This requires the temporal segmentation of inspiration and expiration. Ideally, the source $\mathbf{h}_{\text{in}}$ has a high inspiratory-to-expiratory-*ratio*

$$E_{\text{rat}}(\mathbf{h}_{\text{in}}) = 10 \log \left(\frac{f_{\text{in}}(\mathbf{h}_{\text{in}})}{f_{\text{ex}}(\mathbf{h}_{\text{in}})} \right) \quad \text{(dB)}, \tag{18}$$

whereas $\mathbf{h}_{\text{ex}}$ has a high expiratory-to-inspiratory-*ratio*

$$E_{\text{rat}}(\mathbf{h}_{\text{ex}}) = 10 \log \left(\frac{f_{\text{ex}}(\mathbf{h}_{\text{ex}})}{f_{\text{in}}(\mathbf{h}_{\text{ex}})} \right) \quad \text{(dB)}. \tag{19}$$

Due to the ventilation context, eqs. (16) to (19) are calculated breath-wise and averaged over all breathing cycles, respectively.

2.3.3. Before-and-after comparison. The mixed sEMG envelopes $\mathbf{s}_j^{\text{env}}$ of each channel $j = 1, \ldots, m$ obtained from eq. (14) represent the activity of all contributing muscles without cardiac artifacts. Therefore, they can be used to evaluate whether and to what extent the separation has increased the similarity to the references. They serve as a baseline for the separation success and allow a before-and-after comparison with all evaluation measures in section 2.3.2. The improvement induced by the separation of the kth source projected to the jth channel can be assessed by the *distortion* improvement

$$\Delta E_{\text{dist}}^{k,j} = E_{\text{dist}}(\mathbf{s}_j^{\text{env}}, \mathbf{r}_{k,j}) - E_{\text{dist}}(\mathbf{h}_k, \mathbf{r}_{k,j}), \tag{20}$$

the *correlation* improvement

$$\Delta E_{\text{corr}}^{k,j} = - \left(E_{\text{corr}}(\mathbf{s}_j^{\text{env}}, \mathbf{r}_{k,j}) - E_{\text{corr}}(\mathbf{h}_k, \mathbf{r}_{k,j}) \right), \tag{21}$$

and the amplitude *ratio* improvement

$$\Delta E_{\text{rat}}^{k,j} = - \left(E_{\text{rat}}(\mathbf{s}_j^{\text{env}}) - E_{\text{rat}}(\mathbf{h}_k) \right) \tag{22}$$

with $k \in \{\text{in}, \text{ex}\}$. We define eqs. (20) to (22) in a way that $\Delta E > 0$ indicates an improvement.

2.3.4. Validation on simulated sEMG signals. The overall validation procedure with simulated sEMG signals is illustrated in fig. 3. It is divided into three parts: First, test and reference signals are generated. The next phase identifies the respiratory activation primitives and reconstructs the mixed sEMG signals with suppressed cardiac artifacts. The third phase uses the ground truth signals, the separation results, the mixed sEMG envelopes and the introduced evaluation and improvement measures (sections 2.3.2 and 2.3.3) to assess the separation performance.

The generation of multiple test settings for extensive verification of different scenarios is based on:

- *Subsets of active muscles:* Employing the sEMG simulation model, explained in section 2.1.2, provides the individual contributions of four different muscle groups (DI, EI, II and RA). Superposing the simulated surface potentials in various combinations generates different recruitment patterns. These patterns simulate patients who recruit only specific muscles for respiration and include cases where inspiration or expiration is passive. Naturally, passive inspiration is only possible for ventilated patients. The contribution of non-contracting muscles is assumed to be zero. In total, 15 different recruitment patterns are simulated.

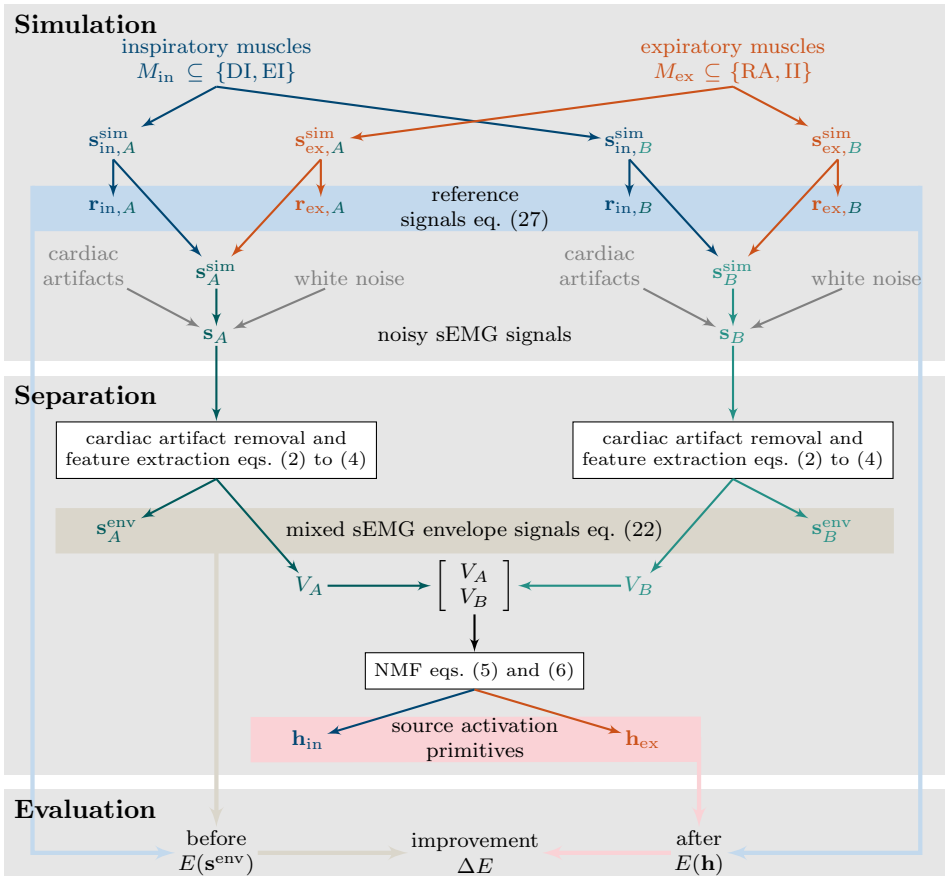

Figure 3: Overview of the validation procedure. In the simulation phase, the sEMG model described in section 2.1.2 is used to simulate inspiratory and expiratory surface potentials at different electrode positions. Figure 1 illustrates the modeled muscles and channel configurations. Based on this, the ground truth is calculated, and subsequently, the signals are mixed and contaminated with artificial cardiac artifacts and noise. In this stage, varying muscle recruitment patterns, channel configurations, and SNRs generate different test signals, simulating real noisy recordings. In the following phase, signal processing and separation are applied as described in section 2.2. In addition to the activation primitives, the mixed sEMG signal is reconstructed, and its envelope is calculated. Finally, the results *before* and *after* BSS are evaluated and compared using the references and the assessment measures described in sections 2.3.2 and 2.3.3.

- *Configurations of channels:* Three configurations, only channel A, only channel B, and both are chosen. The single-channel configurations imitate the scenario in which disturbances corrupt one channel or only one channel is recorded.
- *Signal-to-noise ratios (SNR):* White noise is added in six different SNRs from $-3\,\mathrm{dB}$ to $12\,\mathrm{dB}$ with

$$\mathrm{SNR} = 10\log\left(\frac{\mathbb{E}\{\mathrm{EMG}^2\}}{\mathbb{E}\{\mathrm{noise}^2\}}\right) \quad (\mathrm{dB}). \tag{23}$$

  This range imitates the amplitudes of the clinical data.

Artificial cardiac artifacts are added to each generated signal, as explained in section 2.1.2.

When defining appropriate references for the source activation primitives, some assumptions have to be made, because these inspiratory and expiratory primitives are virtual source signals which are not used or acquired in the employed sEMG simulation model. For this reason, the reference signals are formed based on the simulated surface potentials $\mathbf{s}^{\mathrm{sim}}_{M,j}$ associated with the respective source and channel. More precisely, the references for each channel $j \in \{A, B\}$ and each source $k \in \{\mathrm{in}, \mathrm{ex}\}$ are obtained from

$$\mathbf{r}_{k,j} = \mathrm{env}\left(\mathbf{s}^{\mathrm{sim}}_{k,j}\right) = \mathrm{env}\left(\sum_{M_k} \mathbf{s}^{\mathrm{sim}}_{M_k,j}\right), \tag{24}$$

where $M_{\mathrm{in}} \subseteq \{\mathrm{DI}, \mathrm{EI}\}$ and $M_{\mathrm{ex}} \subseteq \{\mathrm{RA}, \mathrm{II}\}$ are the muscles recruited in the considered test dataset. The reference surface potentials are without additional cardiac artifacts, thus no removal in the wavelet domain is required. In conclusion, the reference signals in eq. (24) correspond exactly to the envelopes of the surface potentials we would measure without crosstalk, cardiac artifacts, or noise. It is noteworthy that we do not explicitly evaluate the removal of cardiac artifacts. However, if artifact residuals are still present in the separated signals, this also leads to a degraded performance evaluation because the similarity to the reference decreases.

2.3.5. Validation on clinical sEMG signals. The proposed procedure is also applied to twelve clinical sEMG datasets. Despite the lack of ground truth, a limited quantitative evaluation is possible. Therefore, this work attempts to use the transdiaphragmatic pressure p_{di} [48] to evaluate the clinical signals' separation success. The pressure p_{di} is an accepted clinical monitor for the patient's breathing behavior. Negative strokes, compared to the baseline pressure, indicate diaphragmatic activity. However, it is an invasive and error-prone method and requires adequate catheter positioning in the esophagus and stomach [49]. Cardiac artifacts also contaminate p_{di} but can be removed using a template subtraction approach [50].

For quantitative validation, two clinical experts have segmented active inspirations in p_{di}. Meanwhile, they were blinded to the sEMG recordings. The intersection of both experts' segmentations serves as a reference for applying eqs. (18) and (19). Consequently, the measure E_{rat} can be calculated for the separation results of each patient, channel and source as explained in section 2.3.2.

3. Results

This section presents the obtained source separation results. At first, the simulated surface potentials are shown and subsequently used in the second part for the proposed

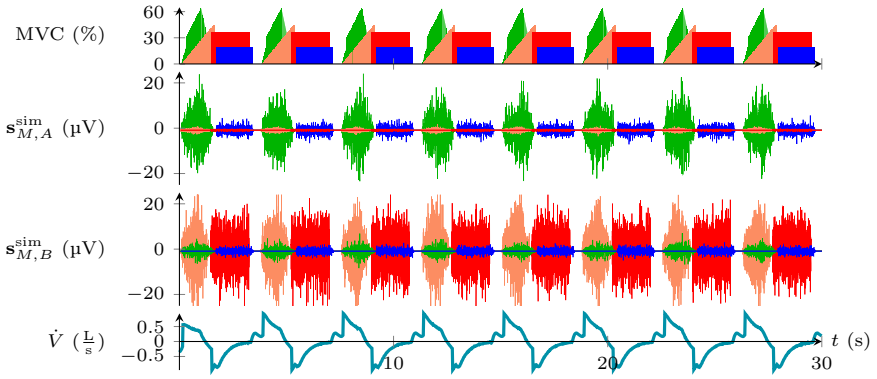

Figure 4: Simulated sEMG signals. The upper row visualizes the presumed muscle load curves in percent of the maximum voluntary contraction level (MVC) for the diaphragm (DI), abdominal muscles (RA), external (EI), and internal (II) intercostal muscles (relative values from 0 to 1, with 1 indicating maximum voluntary contraction). The second and third plot show the simulated surface potentials $\mathbf{s}^{\text{sim}}_{M,A}$ and $\mathbf{s}^{\text{sim}}_{M,B}$ for $M \in \{\text{DI}, \text{RA}, \text{EI}, \text{II}\}$. The scheme in fig. 1 illustrates the electrode positions corresponding to channel A and B. The bottom row shows the simulated airflow obtained from solving eq. (1), used for initializing the activation matrix H as stated in eq. (6).

procedure's quantitative validation. Finally, the algorithm is applied to clinical datasets, and the results are evaluated based on expert annotations.

3.1. Separation of sEMG simulations

Figure 4 shows the employed surface potential simulations of the four most crucial respiratory muscle groups. The muscle load curves (first row) picture that the muscles are not contracting entirely synchronously in our simulation setup. Especially, the activity onset and offset are not the same for the inspiratory muscles $M_{\text{in}} = \{\text{DI}, \text{EI}\}$ nor for the expiratory muscles $M_{\text{ex}} = \{\text{RA}, \text{EI}\}$. This test setup provides a roughly realistic breathing pattern with reasonable complexity regarding the demanded BSS. Due to proximity, DI and RA are most prominent in channel A, whereas EI and II show large amplitudes in channel B. On the other hand, all muscles contribute to both channels. For example, the crosstalk of DI and RA in channel B is significant due to the muscles' size and large electrode distances. As explained in section 2.3.4, multiple test recordings with varying recruitment patterns are generated from the surface potentials in fig. 4.

Figure 5 presents the results of the before-and-after comparison and evaluated improvement measures, described in section 2.3.2. The scatter and the box plots validate the improvement of E_{dist} and E_{corr} by applying BSS for most samples. There are some samples where $E_{\text{dist}}(\mathbf{h}) \approx E_{\text{dist}}(\mathbf{s}^{\text{env}})$ or $E_{\text{corr}}(\mathbf{h}) \approx E_{\text{corr}}(\mathbf{s}^{\text{env}})$, which implies that the separation was not entirely successful, but the separation results are not worse than the simulated mixed signals. Nevertheless, the source separation algorithm can improve the distortion E_{dist} for most samples. The correlation has neither improved nor deteriorated in the denoising case as $\Delta E_{\text{corr}} \approx 0$ for almost all samples of all SNRs. Here, only inspiratory *or* expiratory muscles are active. Thus, the mixed signal $\mathbf{s}^{\text{env}}$

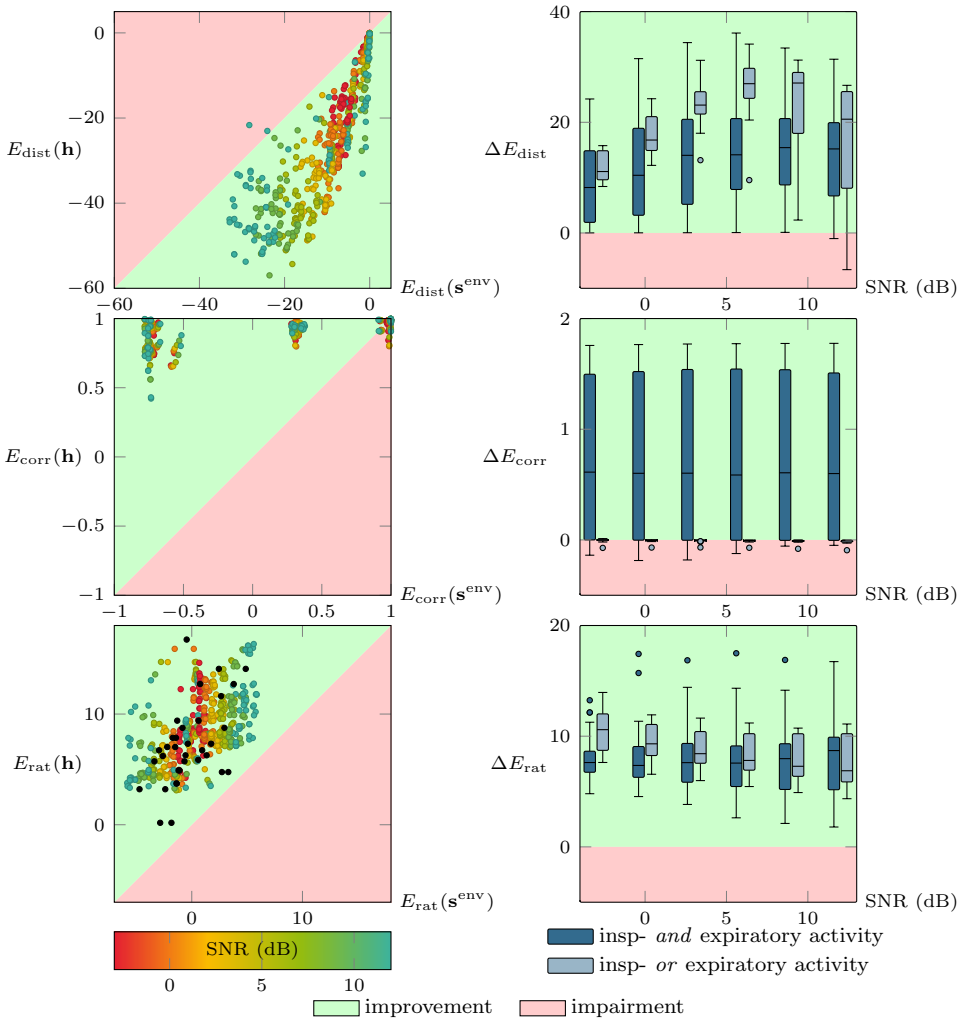

Figure 5: Quantitative evaluation of BSS success using simulated sEMG signals. The figure presents three different evaluation measures, from top to bottom: distortion E_{dist}, correlation E_{corr}, and the success of separating inspiration and expiration E_{rat}. Single- and two-channel datasets are evaluated on different muscle recruitment combinations with SNRs in $-3\,\text{dB}$ to $12\,\text{dB}$ (see section 2.3.4). The left column compares $E(\mathbf{s}^{\text{env}})$ (before) and $E(\mathbf{h})$ (after). The right column summarizes all samples in the corresponding improvement measures ΔE for increasing SNRs. These plots distinguish between the results referring to, first, active inspiration *and* expiration (separation case) and, secondly, only one active source (denoising case). In all plots, green areas indicate improvements for each validation measure. Note that the definitions of E_{corr} and E_{rat} imply the more, the better relations, whereas the distortion E_{dist} is defined oppositely. That causes the flipped background categorization. The measure E_{rat} is also evaluated for the clinical datasets (•), as explained in section 3.2. For this purpose, clinical experts have segmented the respiratory phases based on invasive pneumatic recordings. They were blind to the source separation results.

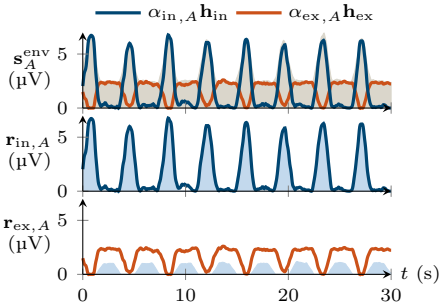

(a) Channel A with two muscles active: $M_{\text{in}} = \{\text{DI}\}$ and $M_{\text{ex}} = \{\text{RA}\}$

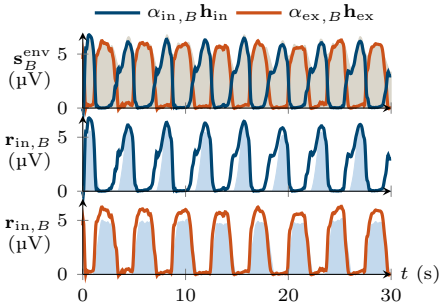

(b) Channel B with four muscles active: $M_{\text{in}} = \{\text{DI}, \text{EI}\}$ and $M_{\text{ex}} = \{\text{RA}, \text{II}\}$

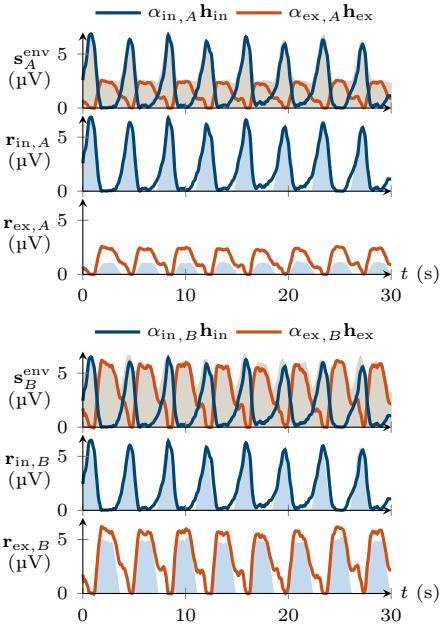

(c) Channel A (first three rows) and B (last three rows) with four muscles active: $M_{\text{in}} = \{\text{DI}, \text{EI}\}$ and $M_{\text{ex}} = \{\text{RA}, \text{II}\}$. As only two sources are separated, all blue and all orange lines are equal up to a scaling factor, respectively.

Figure 6: Exemplary separation results on simulated sEMG recordings. This figure shows the identified inspiratory (— $\mathbf{h}_{\text{in}}$) and expiratory (— $\mathbf{h}_{\text{ex}}$) activation primitives in single-channel (fig. 6a and fig. 6b) and two-channel (fig. 6c) setups. The background of the first row in each panel shows the mixed sEMG envelope signal ($\mathbf{s}^{\text{env}}$) according to eq. (14). The second and the third row compare both estimated source activation primitives and their ground truth ($\mathbf{r}$) obtained from eq. (24), respectively. The source signals $\mathbf{h}_{\text{in}}$ and $\mathbf{h}_{\text{ex}}$ are scaled to fit $\mathbf{s}^{\text{env}}$ according to eqs. (12) and (15).

and the reference signal differ only by additive white noise. Since we compare the signal envelopes, $E_{\text{corr}}(\mathbf{s}^{\text{env}})$ is already very high before separation and can hardly be improved. However, if BSS successfully separates the source signal from noise, the signal is denoised, and $\Delta E_{\text{dist}} > 0\,\text{dB}$ verifies improvement. In the separation case, ΔE_{corr} is widespread but mostly improved. This can be traced back to the broad range of the initial correlation $E_{\text{corr}}(\mathbf{s}^{\text{env}})$, as to be seen in the associated scatterplot in fig. 5. Regarding E_{rat}, all samples fulfill $E_{\text{rat}}(\mathbf{h}) > E_{\text{rat}}(\mathbf{s}^{\text{env}})$ and $E_{\text{rat}}(\mathbf{h}) > 0\,\text{dB}$, which means that the goal of separating inspiration and expiration is successful in all simulated settings. In all cases, the initialization of the matrix H using eq. (6) achieves the mapping of $\mathbf{h}_{\text{in}}$ and $\mathbf{h}_{\text{ex}}$ to the correct inspiratory and expiratory reference signals. Thus, no additional source matching step is necessary, indicating that an airflow-based initialization can solve the standard mapping problem of NMF in this setup.

Figure 6 shows three examples for separating simulated sEMG recordings: Two single-channel and one two-channel setting. In all cases, SNR = 3 dB is chosen. In fig. 6a, only the DI and RA are separated. Here, the separation is of high quality, and the inspiratory reference signal can be reconstructed. The estimated source $\mathbf{h}_{\mathrm{ex}}$ slightly varies because it contains most of the added noise. The results of the second example in fig. 6b are similarly accurate, although the NMF algorithm partially attributes the noise to $\mathbf{h}_{\mathrm{in}}$. Here, the surface potentials of all muscle groups contribute to the sEMG signal. However, EI and II are dominant in channel B, as shown in fig. 4. The same recruitment pattern, with all muscles being active, is shown in fig. 6c, but here, both channels are used. Again, the separation is effective, and the separated sources resemble the references. However, the estimated primitives in figs. 6b and 6c differ even though exactly the same simulated signal was used for channel B. In fig. 6c, the deviation of the shape of $\mathbf{h}_{\mathrm{ex}}$ to its reference is more significant than for $\mathbf{h}_{\mathrm{in}}$, suggesting that the noise is mapped to the expiratory source. This example with multiple channels illustrates that the identified sources are a compromise between all recordings.

The utilized implementation is not performance optimized and runs on a normal desktop PC (i5-8350U CPU). The average run time of the entire algorithm on the simulation data per 30 s signal sections is 0.752 s in the single-channel case and 0.998 s in the two-channel case.

3.2. Separation of clinical sEMG datasets

Figure 7 illustrates four single-channel examples obtained from three different patients. In all cases, the algorithm could separate two alternating sources. Except for some minor differences, the estimated inspiration primitive $\mathbf{h}_{\mathrm{in}}$ correlates with the negative swings in the invasively measured transdiaphragmatic pressure p_{di}. We conclude that the two sources are matched correctly only by the initialization based on the airflow $\dot{V}$.

With two recorded channels of good quality, one can use both for the separation. Figure 8 presents examples obtained from four patients. The datasets differ regarding the sEMG recordings and the flow curves, caused by respiratory activity of the patients and the ventilatory support. As the amplitude of the separated source activation primitives is arbitrary, $\mathbf{h}_{\mathrm{in}}$ and $\mathbf{h}_{\mathrm{ex}}$ are scaled to fit the mixed sEMG signal envelopes $\mathbf{s}_A^{\mathrm{env}}$ and $\mathbf{s}_B^{\mathrm{env}}$, respectively. We conclude that the restriction to only two sources is reasonable for all recordings (figs. 7 and 8) since the linear combination of both estimated activation primitives reproduces both mixed signal envelopes appropriately. Like in the single-channel case, the results in the multi-channel case are plausible: The negative strokes in p_{di} match the inspiratory source activation primitive $\mathbf{h}_{\mathrm{in}}$ for all patients. The dataset in fig. 8a is especially noticeable because the airflow and the detected breaths do not match completely. The likely explanation is patient-ventilator-asynchrony [20]–[22]. Once more, the initialization with the airflow facilitates the source mapping. Additionally, in the case of asynchrony, the algorithm can find additional active or inactive breaths, and the acquired results are reasonable according to the invasively measured pressure p_{di}. The differences of single- and two-channel cases can be examined, when comparing figs. 7c and 8d, showing the single- and two-channel results for the same recording. In fig. 8d, the estimated activation primitives are smoother, and the two sources are separated more clearly than in the single-channel cases. Furthermore, the processed clinical datasets show no disturbing cardiac artifact residuals, neither in the mixed signal envelopes

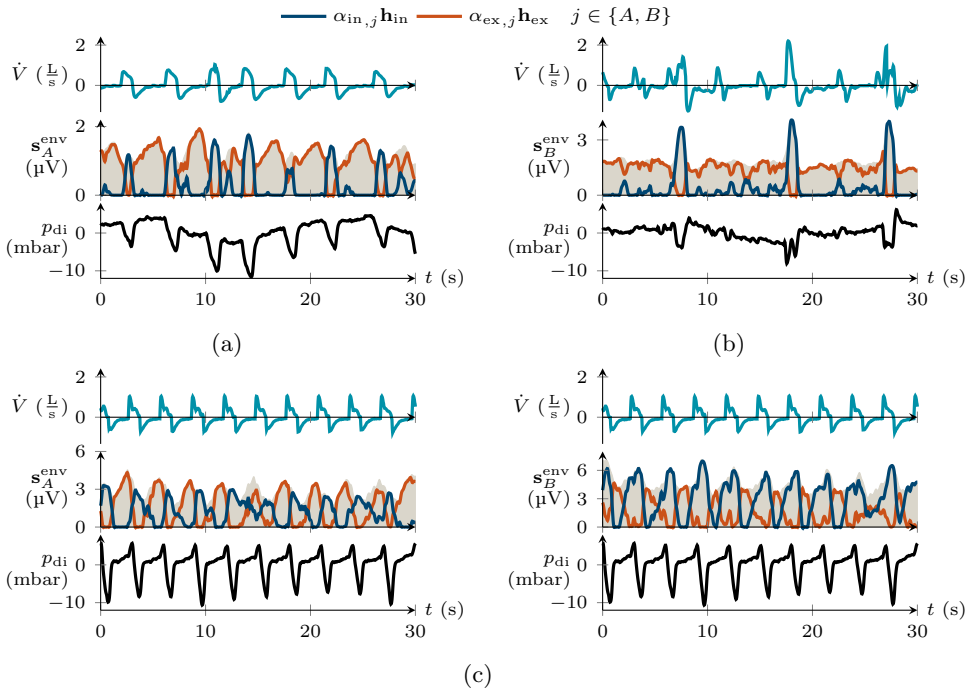

Figure 7: Separation results on two clinical sEMG datasets (single-channel). One differential sEMG recording yields the separated inspiratory (— $\mathbf{h}_{\text{in}}$) and expiratory (— $\mathbf{h}_{\text{ex}}$) activation primitives. The top row examples (figs. 7a and 7b) are recorded from different patients and electrode positions. At the top, the airflow signal $\dot{V}$ is given, used for initializing the source activation primitives. The second row shows the separation results, as well as the mixed signal envelope with suppressed cardiac artifacts (▬ $\mathbf{s}^{\text{env}}$) obtained from eq. (12). The primitives are scaled according to eqs. (12) and (15). The invasively measured transdiaphragmatic pressure p_{di} is given at the bottom. In the latter, negative strokes indicate the patient's inspiratory effort. The left and right plot in fig. 7c correspond to the same patient and the same time segment of the recording, but differ regarding the utilized sEMG channel. The results of both single-channel cases can be compared to results in fig. 8d, where the same recording in a two-channel scenario is processed.

nor in the separated source activation primitives. Consequently, the cardiac artifact removal performed robustly for all patients and preserved the sEMG wavelet spectrum, such that BSS can still be successful.

For each patient, channel, and source in figs. 7 and 8 and six additional patients, the measure E_{rat} is calculated as explained in section 2.3.5. The blue circles in the bottom left plot of fig. 5 show the results. We can make two observations: First, the proposed procedure improves the ratio of both sources E_{rat} in all cases. Second, the validation based on simulated sEMG signals reflects the true measurements properly because the outcome of E_{rat} is in the same range of values.

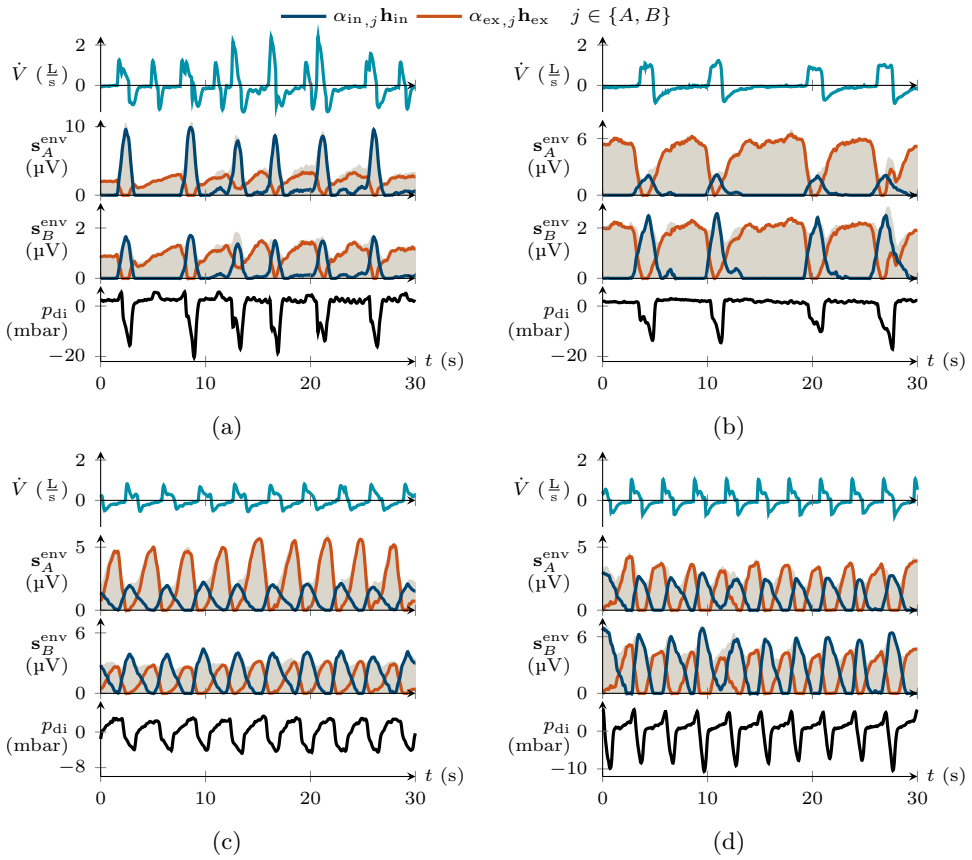

Figure 8: Separation results on two-channel clinical sEMG datasets. The subfigures present the separation results of four different patients with varying breathing patterns. In all datasets, two sEMG recording channels are available. The rows from top to bottom show the airflow $\dot{V}$, the mixed sEMG signal envelopes ($\mathbf{s}^{\mathrm{env}}$) according to channel A and channel B obtained from eq. (12), and finally, the transdiaphragmatic pressure p_{di}. Again, the separated source activation primitives for inspiration ($\mathbf{h}_{\mathrm{in}}$) and expiration ($\mathbf{h}_{\mathrm{ex}}$) are plotted, where the signals in both rows are equal, up to the scaling factors obtained from eqs. (12) and (15). Negative strokes in the invasively measured transdiaphragmatic pressure indicate the patient's inspiratory effort.

4. Conclusion and outlook

In this article, we have proposed a new method for separating inspiratory and expiratory activity in respiratory surface EMG recordings of patients under mechanical ventilation. The presented algorithm combines standard tools for cardiac artifact removal and BSS. The separation procedure performs robust and without any tuning, training data, or prior knowledge for different patients. A solution for the common problem of initialization and source matching is proposed, using the recorded ventilatory airflow. The proposed algorithm is computationally efficient and applicable

to single-channel and low-density sEMG recordings of the respiratory muscles.

For the quantification of separation success, three evaluation measures are applied on various sEMG simulations with different signal-to-noise ratios. BSS improved or maintained the three quantities in all test datasets and SNRs. Both the *separation* and the *denoising cases* were successful, implying that the proposed algorithm can be applied to respiratory sEMG recordings, regardless of whether active or passive expiration is present in the data. Although there is no ground truth for the separated clinical sEMG datasets, the results appear realistic. Based on the transdiaphragmatic pressure and two experts' segmentations, we have shown that the ratio of the inspiratory-to-expiratory signal power significantly improves for all patients. In simulated and clinical datasets, the cardiac artifact removal was successful for this application, because no cardiac artifact residuals disturb the envelopes or separated source activation primitives. For the simulated signals, the results confirm that the procedure correctly preserves the sEMG signal's energy because the amplitudes of the mixed envelope and the references are similar.

This paper makes several assumptions about the relation between the estimated source signals, generated references, mixed sEMG signal envelopes, and derived wavelet bands. In the underdetermined case, some of these assumptions enabled to solve the source separation problem, and in multi-channel settings, they simplify the separation and potentially compress information. For example, choosing the NMF as BSS algorithm implicitly requires the synchronous activation of each source in all wavelet bands of all channels. On the other hand, estimating only two sources is a strong simplification that might not be sufficient in other datasets. Nevertheless, we have shown that this provides robust results for all tested datasets. Additionally, the representation of the patient's respiratory muscle activity, condensed to only two primitives, could be beneficial in clinical routines because it facilitates interpretation. Especially if only the patient's inspiratory effort is of interest, the algorithm has the potential to fuse information of two or more recordings. We have shown clinical examples where reasonable interpretation of the mixed sEMG envelopes would not be possible, whereas the separation results give insight into the patient's breathing activity.

We have made two strong assumptions during the validation. First, eq. (11) implicitly assumes that both references $\mathbf{r}_{\mathrm{in},A}$ and $\mathbf{r}_{\mathrm{in},B}$ are equal up to a scaling factor. The same applies to the expiratory references, but it is not precisely accurate in either case, in none of the simulated two-channel settings. That means the proposed algorithm never had a chance to reproduce all references of multiple channels exactly. Instead, estimated primitives resembling both references as much as possible would be the best outcome. Furthermore, from eqs. (11) and (12) follows that the sum of $\mathbf{r}_{\mathrm{in}}$ and $\mathbf{r}_{\mathrm{ex}}$ should approximate $\mathbf{s}^{\mathrm{env}}$ (of both channels). Even if cardiac artifacts are neglected, that is also inaccurate in the simulated settings because white noise was added in advance. Thus, excellent separation results that almost fulfill eq. (12) could not match the reference signals precisely because the algorithm maps the noise to one or both estimated source activations. Thus, very good separation results that almost fulfilled eq. (12) could not exactly match the reference signals, because the added noise is mapped to one or both estimated source activations. In real data, this might not be a drawback, but it is more difficult to achieve good results in the validation. However, both inaccurate assumptions make the data in the performance evaluation more realistic. And despite the limitations, all evaluation measures showed improvements in test datasets, and we conclude the proposed separation procedure

can be rated as a success.

An open question is the algorithm's performance on long-term measurements, where the source properties might change over time due to varying breathing behavior and muscle recruitment. Furthermore, clinical applications usually require real-time procedures. For addressing both challenges, an online implementation would be necessary [51], [52].

Acknowledgement

We want to acknowledge Drägerwerk AG & Co. KGaA, Lübeck, Germany, for the financial support of the clinical trial, the data acquisition and evaluation. Special thanks go to Marcus Eger and Thomas Handzsuj (Drägerwerk AG & Co. KGaA, Lübeck, Germany) for fruitful discussions and for initiating the contact between the University of Lübeck and the Charité Berlin. We would also like to thank the reviewers for their time, constructive comments, and excellent questions.

References

[1] G. Bellani *et al.*, "Measurement of diaphragmatic electrical activity by surface electromyography in intubated subjects and its relationship with inspiratory effort," *Respiratory Care*, vol. 63, no. 11, pp. 1341–1349, Nov. 2018. DOI: 10.4187/respcare.06176.

[2] J. Graßhoff *et al.*, "Surface EMG-based quantification of inspiratory effort: A quantitative comparison with pes," *Critical Care*, vol. 25, no. 1, Dec. 2021. DOI: 10.1186/s13054-021-03833-w.

[3] N. Dimitrova, G. Dimitrov, and O. Nikitin, "Neither high-pass filtering nor mathematical differentiation of the EMG signals can considerably reduce cross-talk," *Journal of Electromyography and Kinesiology*, vol. 12, no. 4, pp. 235–246, Aug. 2002. DOI: 10.1016/s1050-6411(02)00008-1.

[4] A. Holobar and D. Farina, "Blind source identification from the multichannel surface electromyogram," *Physiological Measurement*, vol. 35, no. 7, R143–R165, Jun. 2014. DOI: 10.1088/0967-3334/35/7/r143.

[5] C. J. De Luca, A. Adam, R. Wotiz, L. D. Gilmore, and S. H. Nawab, "Decomposition of surface EMG signals," *Journal of Neurophysiology*, vol. 96, no. 3, pp. 1646–1657, Sep. 2006. DOI: 10.1152/jn.00009.2006.

[6] A. Holobar and D. Zazula, "Multichannel blind source separation using convolution kernel compensation," *IEEE Transactions on Signal Processing*, vol. 55, no. 9, pp. 4487–4496, Sep. 2007. DOI: 10.1109/tsp.2007.896108.

[7] Y. Wen *et al.*, "A convolutional neural network to identify motor units from high-density surface electromyography signals in real time," *Journal of Neural Engineering*, vol. 18, no. 5, p. 056 003, Apr. 2021. DOI: 10.1088/1741-2552/abeead.

[8] F. Negro, S. Muceli, A. M. Castronovo, A. Holobar, and D. Farina, "Multi-channel intramuscular and surface EMG decomposition by convolutive blind source separation," *Journal of Neural Engineering*, vol. 13, no. 2, p. 026 027, Feb. 2016. DOI: 10.1088/1741-2560/13/2/026027.

[9] E. Petersen, H. Buchner, M. Eger, and P. Rostalski, "Convolutive blind source separation of surface EMG measurements of the respiratory muscles," *Biomedical Engineering / Biomedizinische Technik*, vol. 62, no. 2, Jan. 2017. DOI: 10.1515/bmt-2016-0092.

[10] S. Muceli, N. Jiang, and D. Farina, "Extracting signals robust to electrode number and shift for online simultaneous and proportional myoelectric control by factorization algorithms," *IEEE Transactions on Neural Systems and Rehabilitation Engineering*, vol. 22, no. 3, pp. 623–633, May 2014. DOI: 10.1109/tnsre.2013.2282898.

[11] M. C. Tresch, V. C. K. Cheung, and A. d'Avella, "Matrix factorization algorithms for the identification of muscle synergies: Evaluation on simulated and experimental data sets," *Journal of Neurophysiology*, vol. 95, no. 4, pp. 2199–2212, Apr. 2006. DOI: 10.1152/jn.00222.2005.

[12] A. B. Ajiboye and R. F. Weir, "Muscle synergies as a predictive framework for the EMG patterns of new hand postures," *Journal of Neural Engineering*, vol. 6, no. 3, p. 036 004, May 2009. DOI: 10.1088/1741-2560/6/3/036004.

[13] M. H. Soomro, S. Conforto, G. Giunta, S. Ranaldi, and C. D. Marchis, "Comparison of initialization techniques for the accurate extraction of muscle synergies from myoelectric signals via nonnegative matrix factorization," *Applied Bionics and Biomechanics*, vol. 2018, pp. 1–10, 2018. DOI: 10.1155/2018/3629347.

[14] A. Ebied, E. Kinney-Lang, L. Spyrou, and J. Escudero, "Evaluation of matrix factorisation approaches for muscle synergy extraction," *Medical Engineering & Physics*, vol. 57, pp. 51–60, Jul. 2018. DOI: 10.1016/j.medengphy.2018.04.003.

[15] M. F. Rabbi *et al.*, "Non-negative matrix factorisation is the most appropriate method for extraction of muscle synergies in walking and running," *Scientific Reports*, vol. 10, no. 1, May 2020. DOI: 10.1038/s41598-020-65257-w.

[16] Y. Kim, S. Stapornchaisit, M. Miyakoshi, N. Yoshimura, and Y. Koike, "The effect of ICA and non-negative matrix factorization analysis for EMG signals recorded from multi-channel EMG sensors," *Frontiers in Neuroscience*, vol. 14, Dec. 2020. DOI: 10.3389/fnins.2020.600804.

[17] H. Hanawa *et al.*, "Classification of abnormal muscle synergies during sit-to-stand motion in individuals with acute stroke," *Measurement: Sensors*, p. 100 055, Jun. 2021. DOI: 10.1016/j.measen.2021.100055.

[18] G. Li, Z. Li, J. Li, Y. Liu, and H. Qiao, "Muscle synergy-based planning and neural-adaptive control for a prosthetic arm," *IEEE Transactions on Artificial Intelligence*, pp. 1–1, 2021. DOI: 10.1109/tai.2021.3091038.

[19] M. L. Duiverman *et al.*, "Reproducibility and responsiveness of a noninvasive EMG technique of the respiratory muscles in COPD patients and in healthy subjects," *Journal of Applied Physiology*, vol. 96, no. 5, pp. 1723–1729, May 2004. DOI: 10.1152/japplphysiol.00914.2003.

[20] G. Carteaux *et al.*, "Patient-ventilator asynchrony during noninvasive ventilation: A bench and clinical study," *Chest*, vol. 142, no. 2, pp. 367–376, Aug. 2012. DOI: 10.1378/chest.11-2279.

[21] A. A. Koopman *et al.*, "Transcutaneous electromyographic respiratory muscle recordings to quantify patient–ventilator interaction in mechanically ventilated children," *Annals of Intensive Care*, vol. 8, no. 1, Jan. 2018. DOI: 10.1186/s13613-018-0359-9.

[22] L. Estrada, L. Sarlabous, M. Lozano-Garcia, R. Jane, and A. Torres, "Neural offset time evaluation in surface respiratory signals during controlled respiration," in *2019 41st Annual International Conference of the IEEE Engineering in Medicine and Biology Society (EMBC)*, IEEE, Jul. 2019. DOI: 10.1109/embc.2019.8856767.

[23] E. Petersen, J. Graßhoff, M. Eger, and P. Rostalski, "Surface EMG-based estimation of breathing effort for neurally adjusted ventilation control," *IFAC-PapersOnLine*, vol. 53, no. 2, pp. 16 323–16 328, 2020. DOI: 10.1016/j.ifacol.2020.12.654.

[24] T. Abe, N. Kusuhara, N. Yoshimura, T. Tomita, and P. A. Easton, "Differential respiratory activity of four abdominal muscles in humans," *Journal of Applied Physiology*, vol. 80, no. 4, pp. 1379–1389, Apr. 1996. DOI: 10.1152/jappl.1996.80.4.1379.

[25] R. V. Lourenco and E. P. Mueller, "Quantification of electrical activity in the human diaphragm," *Journal of Applied Physiology*, vol. 22, no. 3, pp. 598–600, Mar. 1967. DOI: 10.1152/jappl.1967.22.3.598.

[26] E. P. Mueller and R. V. Lourenco, "On-line subtraction of the cardiac activity from the esophageal electromyogram of the diaphragm," *IEEE Transactions on Biomedical Engineering*, vol. BME-15, no. 2, pp. 115–118, Apr. 1968. DOI: 10.1109/tbme.1968.4502547.

[27] E. Petersen, J. Sauer, J. Graßhoff, and P. Rostalski, "Removing cardiac artifacts from single-channel respiratory electromyograms," *IEEE Access*, vol. 8, pp. 30 905–30 917, 2020. DOI: 10.1109/access.2020.2972731.

[28] D. D. Lee and H. S. Seung, "Algorithms for non-negative matrix factorization," *Advances in Neural Information Processing Systems*, vol. 13, pp. 556–562, 2001.

[29] E. Petersen and P. Rostalski, "A comprehensive mathematical model of motor unit pool organization, surface electromyography, and force generation," *Frontiers in Physiology*, vol. 10, Mar. 2019. DOI: 10.3389/fphys.2019.00176.

[30] E. Petersen, *semgsim*, https://github.com/ime-luebeck/semgsim, 2021.

[31] R. Sameni, *OSET: The open-source electrophysiological toolbox*, version 3.14, `http://www.oset.ir`, 2018.

[32] P. McSharry, G. Clifford, L. Tarassenko, and L. Smith, "A dynamical model for generating synthetic electrocardiogram signals," *IEEE Transactions on Biomedical Engineering*, vol. 50, no. 3, pp. 289–294, Mar. 2003. DOI: `10.1109/tbme.2003.808805`.

[33] J. H. T. Bates, *Lung Mechanics: An Inverse Modeling Approach*. Cambridge University Press, 2009.

[34] M. Gazzoni *et al.*, "Quantifying forearm muscle activity during wrist and finger movements by means of multi-channel electromyography," *PLoS ONE*, vol. 9, no. 10, A. Asakura, Ed., e109943, Oct. 2014. DOI: `10.1371/journal.pone.0109943`.

[35] M. Niegowski and M. Zivanovic, "Wavelet-based unsupervised learning method for electrocardiogram suppression in surface electromyograms," *Medical Engineering & Physics*, vol. 38, no. 3, pp. 248–256, Mar. 2016. DOI: `10.1016/j.medengphy.2015.12.008`.

[36] X. Chen, Y. Yuan, S. Cao, X. Zhang, and X. Chen, "A SEMG-force estimation framework based on a fast orthogonal search method coupled with factorization algorithms," *Sensors*, vol. 18, no. 7, p. 2238, Jul. 2018. DOI: `10.3390/s18072238`.

[37] M. Savc and A. Holobar, "Non-negative matrix factorization of simulated high density surface electromyograms reflects both muscle excitation and muscle shortening," *IEEE Access*, vol. 9, pp. 70 548–70 555, 2021. DOI: `10.1109/access.2021.3078644`.

[38] J. C. Pesquet, H. Krim, and H. Carfantan, "Time-invariant orthonormal wavelet representations," *IEEE Transactions on Signal Processing*, vol. 44, no. 8, pp. 1964–1970, 1996. DOI: `10.1109/78.533717`.

[39] J. Pan and W. J. Tompkins, "A real-time QRS detection algorithm," *IEEE Transactions on Biomedical Engineering*, vol. BME-32, no. 3, pp. 230–236, Mar. 1985. DOI: `10.1109/tbme.1985.325532`.

[40] D. L. Donoho and I. M. Johnstone, "Ideal spatial adaptation by wavelet shrinkage," *Biometrika*, vol. 81, no. 3, pp. 425–455, Sep. 1994. DOI: `10.1093/biomet/81.3.425`.

[41] E. Henneman, "Relation between size of neurons and their susceptibility to discharge," *Science*, vol. 126, no. 3287, pp. 1345–1347, 1957. DOI: `10.1126/science.126.3287.1345`.

[42] E. Henneman, G. Somjen, and D. O. Carpenter, "Excitability and inhibitibility of motoneurons of different sizes," *Journal of Neurophysiology*, vol. 28, no. 3, pp. 599–620, 1965. DOI: `10.1152/jn.1965.28.3.599`.

[43] C. J. De Luca and Z. Erim, "Common drive of motor units in regulation of muscle force," *Trends in Neurosciences*, vol. 17, no. 7, pp. 299–305, 1994. DOI: `10.1016/0166-2236(94)90064-7`.

[44] M. Piotrkiewicz and K. S. Türker, "Onion skin or common drive?" *Frontiers in Cellular Neuroscience*, vol. 11, Jan. 2017. DOI: `10.3389/fncel.2017.00002`.

[45] D. Farina and R. Merletti, "A novel approach for precise simulation of the EMG signal detected by surface electrodes," *IEEE Transactions on Biomedical Engineering*, 2001.

[46] C. Lawson and R. J. Hanson, *Solving least squares problems*. SIAM, 1987.

[47] D. Schobben, K. Torkkola, and P. Smaragdis, "Evaluation of blind signal separation methods," in *Proceedings of the Workshop on Independent Component Analysis and Blind Signal Separation*, Aussois, France, 1999, pp. 261–266.

[48] L. Brochard, "Transdiaphragmatic pressure," in *Benito S., Net A. (eds) Pulmonary Function in Mechanically Ventilated Patients. Update in Intensive Care and Emergency Medicine*, Springer, Berlin, Heidelberg, 1991, pp. 52–61. DOI: `10.1007/978-3-642-84209-2_5`.

[49] F. Mojoli *et al.*, "In vivo calibration of esophageal pressure in the mechanically ventilated patient makes measurements reliable," *Critical Care*, vol. 20, no. 1, p. 98, Apr. 2016.

[50] J. Graßhoff, E. Petersen, M. Eger, G. Bellani, and P. Rostalski, "A template subtraction method for the removal of cardiogenic oscillations on esophageal pressure signals," in *Proceedings of the 39th Annual International Conference of the IEEE Engineering in Medicine and Biology Society (EMBC)*, New Jersey, USA: IEEE EMBS, 2017, pp. 2235–2238. DOI: `10.1109/EMBC.2017.8037299`.

[51] K. Kwon, J. W. Shin, and N. S. Kim, "NMF-based speech enhancement using bases update," *IEEE Signal Processing Letters*, vol. 22, no. 4, pp. 450–454, Apr. 2015. DOI: `10.1109/lsp.2014.2362556`.

[52] R. Zhao and V. Y. F. Tan, "Online nonnegative matrix factorization with outliers," *IEEE Transactions on Signal Processing*, vol. 65, no. 3, pp. 555–570, Feb. 2017. DOI: 10.1109/tsp.2016.2620967.